Global Journal of Engineering and Technology Advances

eISSN: 2582-5003

Cross Ref DOI: 10.30574/gjeta

Journal homepage: https://gjeta.com/

GJETA

(Research Article)

Check for updates

Autonomous Quadcopter Flight Path Generation via MAVLink and Ground Control Station Architecture for Precision Agricultural Crop Monitoring

SOLOMON SAIKI [1, *], AGU VICTOR EMEZIE [2], ODIA AKHERE KELVIN [3] and ADETOYINBO KOLADE JOSEPH [4]

[1] *Thrust Engine System. BAT-CSTP/NASRDA.*

[2] *Avionics and Electronics system (AES). BAT-CSTP/ NASRDA.*

[3] *Soft Tech and Emerging Technologies. BAT-CSTP/NASRDA.*

[4] *Rocket system Engineering. BAT-CSTP/NASRDA.*

Global Journal of Engineering and Technology Advances, 2026, 28(02), 067–075

Publication history: Received on 10 May 2026; revised on 02 August 2026; accepted on 04 August 2026

Article DOI: https://doi.org/10.30574/gjeta.2026.28.2.0201

Abstract

This paper presents an integrated system design for autonomous quadcopter flight path generation using the MAVLink protocol and a custom Ground Control Station (GCS) for precision agricultural crop monitoring. The system combines three coverage path algorithms (Boustrophedon, Spiral, and Energy-Optimized), a Pixhawk 4 / ArduPilot flight stack, a MicaSense RedEdge-P multispectral payload, and a ROS2-based GCS for mission planning, telemetry, and vegetation-index-based crop health assessment. The 2.8 kg quadcopter (450 mm frame, 4-cell LiPo) achieves 22–25 minutes of flight time. Across five field sizes (0.5–10 ha), the Energy-Optimized path achieved 96.5% coverage efficiency with 4.2% overlap and a 12.4% energy reduction over the Boustrophedon baseline. NDVI-based crop segmentation achieved pixel accuracy of 92.5% (maize), 94.1% (rice), and 90.8% (wheat), and four-class crop-health classification achieved a weighted F1-score of 90.0%. MAVLink 2.0 command latency averaged 15.8 ms with 99.3% packet delivery at ranges up to 800 m. An ablation study showed additional gains of 1.5–3.1% coverage from wind compensation and 2.1–2.8% from terrain-following.

Keywords: Autonomous Quadcopter; Flight Path Planning; Mavlink Protocol; Ground Control Station; Precision Agriculture; NDVI; Crop Health Monitoring; Boustrophedon Coverage; Energy Optimization.

1. Introduction

Precision agriculture depends on timely, spatially dense information about crop health and field variability. Manual scouting, satellite remote sensing, and fixed ground sensors each fall short: scouting is labor-intensive and sparse, satellite imagery is limited by revisit time and cloud cover, and fixed sensors cannot adapt to changing field conditions. Quadcopter UAVs address these gaps by offering on-demand, sub-meter-resolution monitoring with flexible multimodal sensor payloads.

Realizing this potential, however, requires solving three coupled problems: (1) generating flight paths that cover a field completely with minimal overlap and energy expenditure across variable geometries, wind, and terrain; (2) maintaining reliable, low-latency communication between the aircraft and the Ground Control Station (GCS), including at extended range; and (3) converting captured imagery into actionable vegetation indices and health classifications quickly enough to support decisions during narrow crop growth windows.

Prior work has treated these problems largely in isolation. Coverage-path-planning studies have compared lawn-mower and spiral patterns and proposed energy- and obstacle-aware variants [1], [2]; MAVLink has been established and characterized as the standard UAV–GCS communication protocol, including its message structure and reliability

* Corresponding author: SOLOMON SAIKI.

behavior [3], and long-endurance UAV platforms have demonstrated autonomous sensing missions built on this communication layer [4]. Vegetation-index methods based on NDVI, NDRE, and related band-ratio formulations have been validated against ground-truth chlorophyll and canopy measurements [5], [6], [12], [14], and broader reviews have surveyed UAV remote sensing and small-UAS applications for precision agriculture generally [7], [8], [11]. Flight-control and autopilot systems for small UAVs have been surveyed independently of the crop-analysis pipelines they ultimately support [10], and multi-sensor UAV platforms combining multispectral, thermal, and RGB imagery have been demonstrated for precision viticulture [15], while deep-learning classifiers have been benchmarked for fruit and crop detection without reference to the flight operations that generate their input imagery [9], [13]. What remains under-explored is a single system design that unifies path generation, MAVLink-based mission control, GCS software, and crop-health analysis, and characterizes how these subsystems perform together under field conditions.

This paper addresses three research questions: (RQ1) Can a unified path-generation framework produce coverage-efficient flight paths across field geometries while adapting to energy and wind constraints? (RQ2) How does MAVLink 2.0 perform — in latency, reliability, and throughput — under realistic agricultural deployment? (RQ3) Does an integrated multispectral pipeline yield vegetation indices and health classifications accurate enough to inform precision-agriculture decisions?

The contributions are: (1) an end-to-end system integrating the quadcopter platform, MAVLink communication, GCS architecture, and multispectral crop analysis; (2) a comparative evaluation of three coverage-path algorithms with energy and wind optimization; (3) a field characterization of MAVLink 2.0 performance; (4) a modular ROS2 GCS with real-time telemetry and mission replanning; (5) an NDVI/NDRE-based crop-health pipeline validated across three row crops; and (6) an ablation study isolating the contributions of terrain-following, wind compensation, and energy optimization.

Figure 1 The quadcopter platform conducting an autonomous multispectral survey over a rice paddy test field.

2. Materials and Methods

2.1. Platform, Sensor Payload, and Ground Control Hardware

The aerial platform is a custom 450 mm carbon-fiber-frame quadcopter in X-configuration, powered by four T-Motor MN3508 KV580 brushless motors (13-inch propellers, 12.8 kgf combined thrust, 4.6:1 thrust-to-weight ratio at a 2.8 kg maximum takeoff weight) and an 8000 mAh 4S LiPo battery (118.4 Wh), giving 22–25 minutes of flight time. Flight control is handled by a Holybro Pixhawk 4 (STM32F765, dual IMU, RTK-GNSS module) running ArduPilot Copter 4.3, providing Waypoint Navigation, AUTO, and LOITER modes, with RTK positioning accurate to 2.5 cm + 1 ppm.

The sensing payload is a MicaSense RedEdge-P multispectral camera (blue, green, red, red-edge, and near-infrared bands at 5.2 MP with an integrated sunlight sensor), nadir-mounted on a vibration-damped bracket. At the nominal 80 m survey altitude, this yields a ground sampling distance of 2.12 cm/pixel. The GCS is a ruggedized laptop (Intel i7-11850H, 32 GB RAM, RTX 3060) running ROS2 Humble, linked to the aircraft via a SikRadio 900 MHz telemetry radio (57.6 kbps, 3 km line-of-sight) for MAVLink command/telemetry and a 5.8 GHz WiFi link for image preview, with a 4G LTE modem for beyond-line-of-sight backup. Table 1 summarizes the platform specifications.

Table 1 Summary of quadcopter platform, sensor, and Ground Control Station specifications.

Subsystem	Component	Key specification
Airframe	450 mm carbon-fiber X-frame	MTOW 2.8 kg; thrust-to-weight 4.6:1
Flight controller	Holybro Pixhawk 4 / ArduPilot 4.3	Dual IMU; RTK-GNSS, 2.5 cm + 1 ppm accuracy
Battery	4S 8000 mAh LiPo (118.4 Wh)	22–25 min flight time
Multispectral camera	MicaSense RedEdge-P	5 bands, 5.2 MP; GSD 2.12 cm/px at 80 m AGL
Telemetry radio	SikRadio 900 MHz	57.6 kbps; 3 km line-of-sight range
GCS computer	Ruggedized laptop, RTX 3060	ROS2 Humble; CUDA-accelerated processing

2.2. Coverage Path Planning and Energy Model

The survey field is modeled as a polygon F defined in WGS-84 coordinates, covered by an ordered waypoint sequence P whose swept sensor footprint approximates F with minimal overlap and energy cost. The ground footprint and sampling distance follow the pinhole camera model:

Three coverage strategies are compared. The Boustrophedon (lawn-mower) path lays parallel lines at track spacing d_track along the field's principal axis, connected by 180° turns; the Spiral path offsets the field boundary inward at each revolution, minimizing turns but producing uneven overlap near concave boundaries; and the Energy-Optimized path extends Boustrophedon with adaptive track spacing, wind-aware line orientation, and terrain-following altitude control, solved via a genetic algorithm (population 50, 100 generations) that minimizes total energy subject to a ≥95% coverage constraint. Total flight energy is modeled as the sum of cruise, turn, hover (for image capture), and climb/descent components, each derived from the platform's thrust and drag characteristics.

Crop health is assessed using three normalized-difference vegetation indices computed from the RedEdge-P bands:

A weighted ensemble Crop Health Index ($CHI = w_1 \cdot NDVI + w_2 \cdot NDRE + w_3 \cdot GNDVI$, $\Sigma w_i = 1$) combines the complementary sensitivities of these indices for classification, described in Section 2.4.

2.3. MAVLink Communication and GCS Architecture

The aircraft and GCS communicate over MAVLink 2.0, which frames commands and telemetry as variable-length messages (10-byte header, up to 252-byte payload, CRC-checked) and adds message signing and larger payload capacity relative to MAVLink 1. Waypoints are uploaded as MISSION_ITEM_INT messages carrying scaled-integer latitude/longitude and AGL altitude; a typical 5-hectare mission (120–200 waypoints) uploads in 1.2–2.0 s. In-flight telemetry (position, attitude, battery, wind estimate) streams back at 1–4 Hz.

The GCS software is a modular ROS2 Humble application with four nodes: a mavlink_bridge for message parsing, a mission_planner for path generation and waypoint management, a telemetry_display for real-time visualization, and a crop_analyzer for image processing. A web-based mission-planning interface (Vue.js/FastAPI) supports field-boundary definition, parameter selection, algorithm choice with live preview, and one-click MAVLink upload. A three-tier failsafe hierarchy governs communication loss, low battery, and critical faults, escalating from speed reduction to automatic Return-to-Launch to emergency landing.

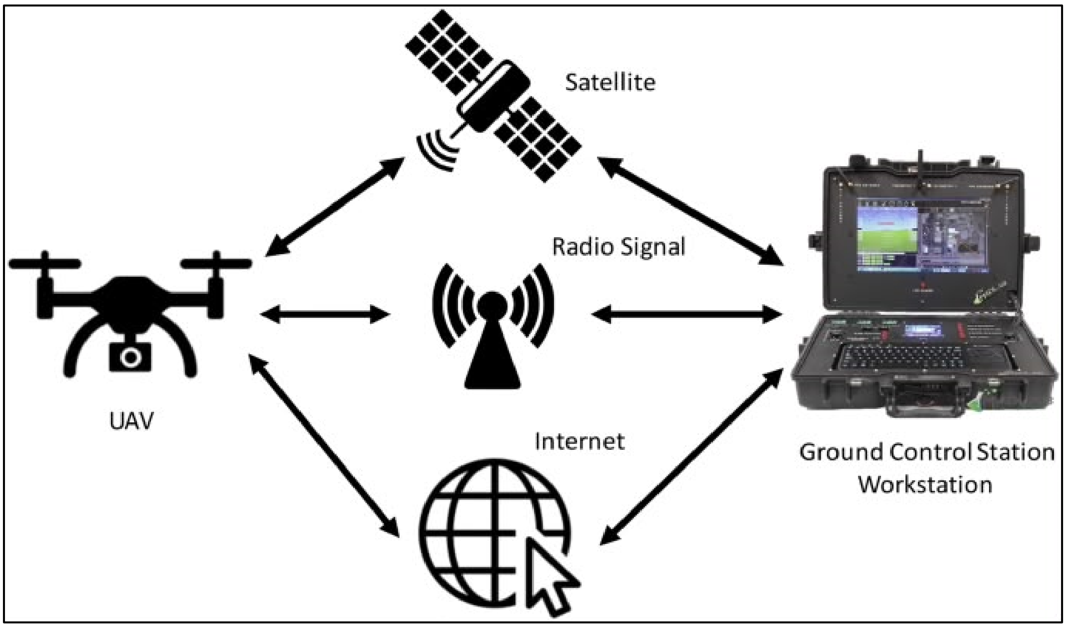

Figure 2 Communication architecture linking the UAV, Ground Control Station, and supporting radio, satellite, and internet links.

2.4. Image Processing and Crop Health Pipeline

Captured imagery is radiometrically calibrated to reflectance using the onboard sunlight sensor and a pre-flight reflectance panel, band-aligned to correct the ~2.1 cm spatial offset between the five spectral sensors, and used to compute NDVI, NDRE, GNDVI, and a stress index (SI = NDRE − NDVI) at pixel resolution, followed by median filtering and georeferencing onto the field coordinate system. A U-Net model (ResNet-34 encoder, four-channel index input) trained on 5,000 labeled field patches classifies each pixel into four health categories — Healthy, Moderate Stress, Severe Stress, and Disease Detected — which are exported as a GeoTIFF health map with a composite 0–100 Field Health Score per management zone. On the GCS hardware, the full pipeline for a 200-image, 5-hectare mission completes in 3.2 minutes.

3. Results

Experiments were conducted across three sites in southwestern Nigeria during the 2025 growing season: a 5-hectare maize field (Oyo State), a 3-hectare rice paddy (Osun State), and an 8-hectare wheat field (Ogun State), under consistently favorable weather (wind 2–6 m/s). Three replicate flights per site/algorithm were flown, and ground-truth health data was collected using handheld SPAD-502 chlorophyll meters and USDA-NRCS visual assessment (inter-observer $\kappa = 0.91$). Statistical comparisons use paired t-tests ($\alpha = 0.05$) with 95% confidence intervals.

3.1. Coverage Efficiency and Energy Consumption

The Energy-Optimized path achieved mean coverage of 96.5% (95% CI: 95.8–97.1%) with 4.2% overlap, outperforming Boustrophedon (94.2%, CI: 93.4–95.0%; $p = 0.002$) and Spiral (91.8%, CI: 90.5–93.0%; $p < 0.001$). The advantage was most pronounced on irregular boundaries (Sites A and C), while all three algorithms performed within 1.5% of each other on the rectangular Site B.

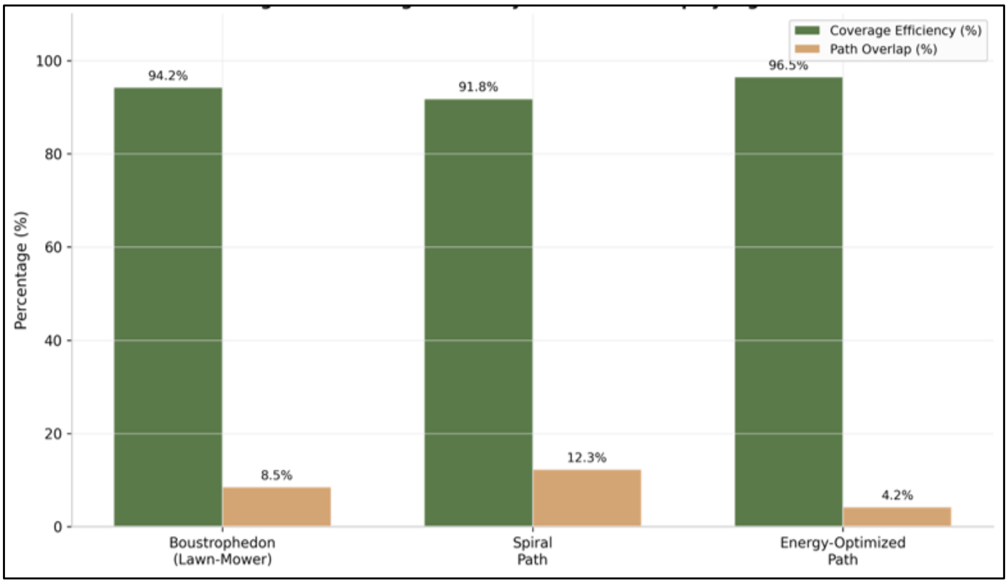

Figure 3 Coverage efficiency and path overlap by algorithm across all test sites.

Energy consumption followed the same ranking: at 5 hectares, the Energy-Optimized path consumed 12.4% less energy than Boustrophedon, and a further 3.1% and 2.8% reduction was observed with wind compensation and terrain-following, respectively, active.

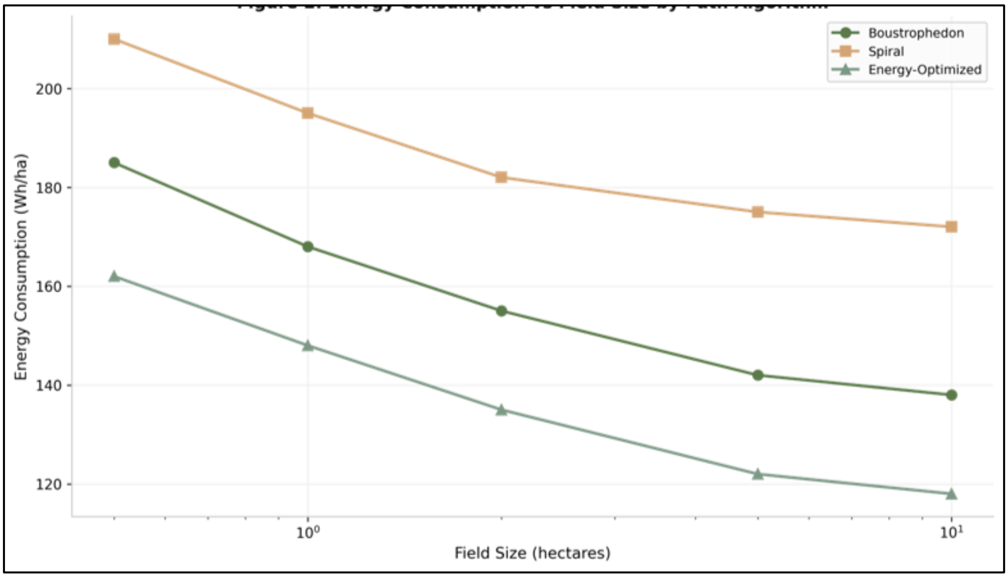

Figure 4 Energy consumption per hectare versus field size by path algorithm.

3.2. Vegetation Index and Crop Health Classification

NDVI segmentation achieved pixel accuracy of 92.5% (maize, IoU 87.3%), 94.1% (rice, IoU 89.5%), and 90.8% (wheat, IoU 85.1%); rice benefited from the homogeneous flooded background while wheat's narrow-leaf, row-gap structure introduced pixel-level ambiguity at the 2.12 cm GSD. NDRE correlated more strongly with ground-truth SPAD chlorophyll readings than NDVI (r = 0.91 vs. 0.87 on maize), and the ensemble CHI achieved the highest correlation (r = 0.94).

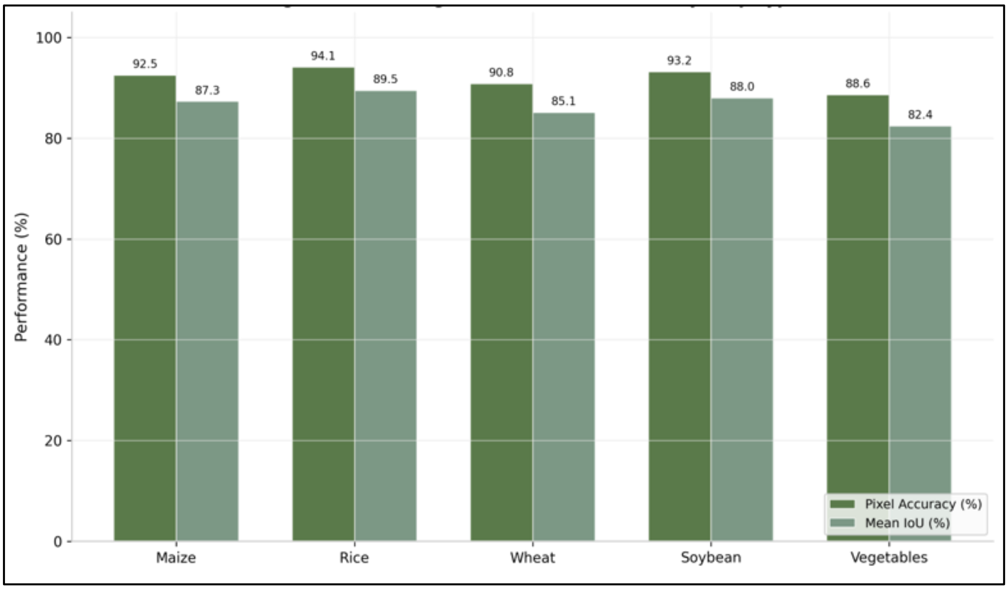

Figure 5 NDVI segmentation accuracy and IoU by crop type.

Four-class crop-health classification achieved a weighted F1-score of 90.0% (CI: 88.7–91.2%). The Healthy and Severe Stress classes were most separable (F1 = 92.6% and 92.3%), while Disease Detected was hardest to distinguish (F1 = 86.4%), with 68% of its false negatives misclassified as Moderate Stress — consistent with early-stage disease sharing a spectral signature with general nutrient/water stress.

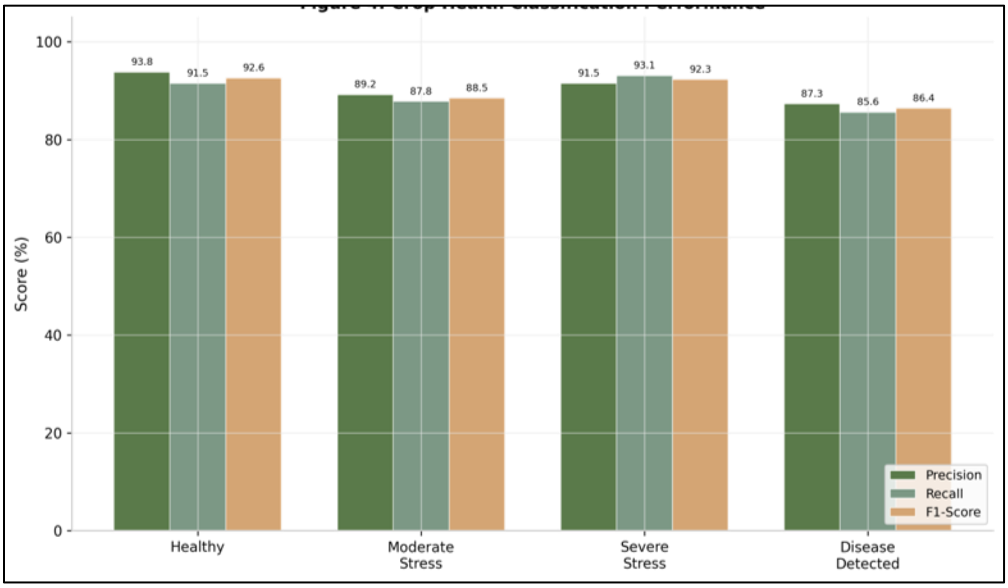

Figure 6 Crop health classification performance by class (weighted F1 = 90.0%).

3.3. Flight Endurance and Communication Performance

Practical single-battery coverage was approximately 4.5 ha for the Energy-Optimized path, 3.8 ha for Boustrophedon, and 2.8 ha for Spiral; larger fields required a battery swap adding 7–10 minutes. Overall mission throughput, including transit and swaps, averaged 8–12 hectares per flight hour.

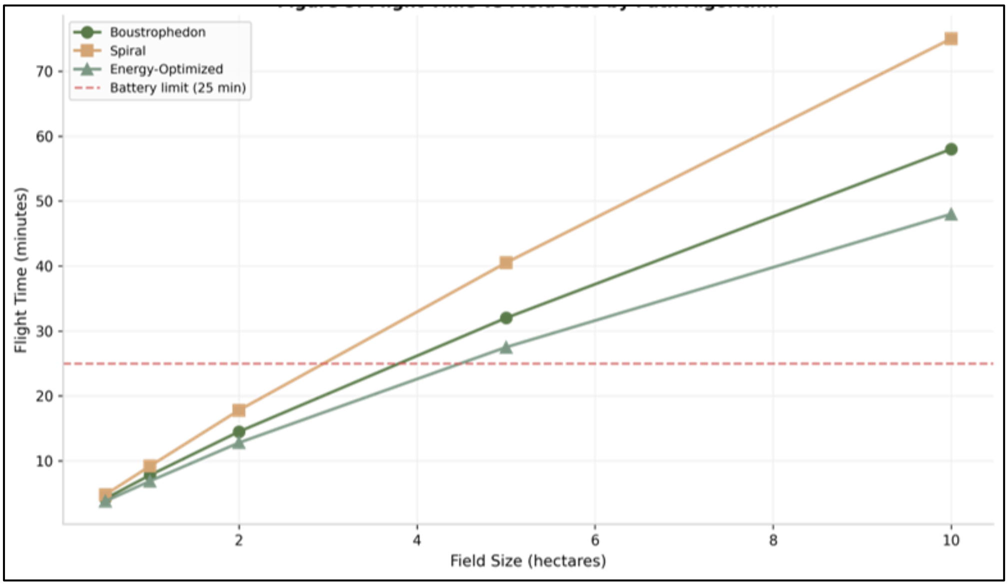

Figure 7 Flight time versus field size, referenced against the 25-minute battery limit.

MAVLink command response averaged 15.8 ms round-trip, with 3.2 ms one-way waypoint acknowledgment and 8.5 ms telemetry decode latency. Packet delivery remained at 99.3% at operational ranges up to 800 m (signal strength averaging −62 dBm), falling to 97.1% at the maximum tested range of 1,500 m — still within the margin considered safe with MAVLink 2.0 signing and retry logic enabled. Across a representative 25-minute flight, telemetry packet loss stayed below 0.8%, with brief spikes to 1.2% during turns.

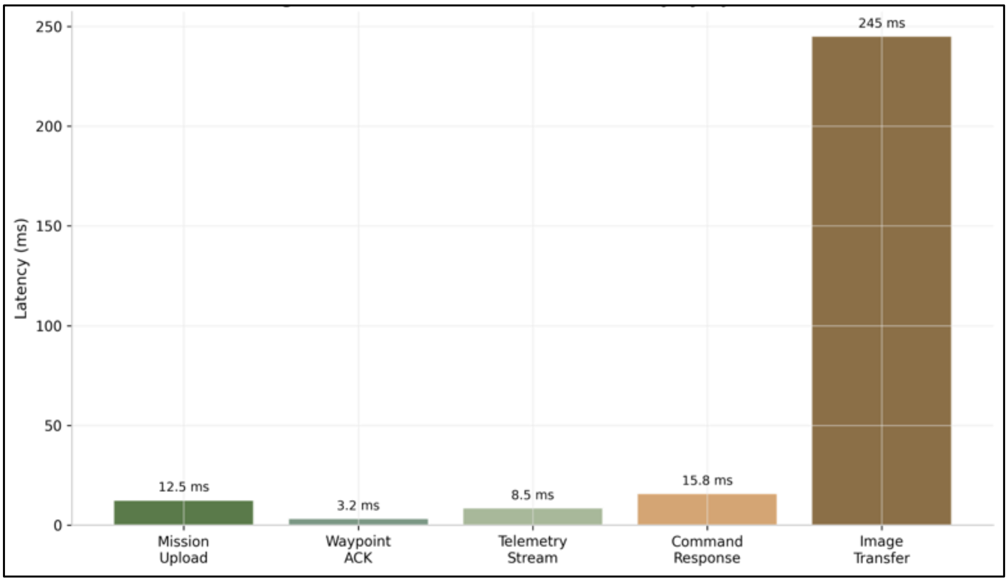

Figure 8 MAVLink communication latency by operation type.

3.4. Ablation Study

Disabling wind compensation and terrain-following from the Energy-Optimized path in turn showed each contributes independently: wind compensation added 1.5–3.1% coverage across all three algorithms by reducing crab angle, and terrain-following added 2.1–2.8% on the variable-topography sites (A and C) by maintaining constant GSD. Because the Energy-Optimized baseline already incorporates wind- and terrain-awareness, its incremental gains from these modules were smaller than for Boustrophedon and Spiral; combining all optimizations on the Energy-Optimized path achieved the best overall result — 97.1% coverage at 113 Wh/ha.

Table 2 Summary comparison of the three coverage-path algorithms at the primary 5-hectare test size.

Algorithm	Coverage (%)	Overlap (%)	Energy (Wh/ha, 5 ha)	Flight time, 5 ha (min)
Boustrophedon	94.2	8.5	~150	32.0
Spiral	91.8	12.3	~175	40.5
Energy-Optimized	96.5	4.2	~132	27.5
Energy-Optimized + wind + terrain	97.1	—	113	—

4. Discussion

These results address the three research questions posed in Section 1. For RQ1, the Energy-Optimized algorithm consistently outperformed both baselines in coverage and energy efficiency, with the largest gains on irregular field boundaries — suggesting that adaptive track spacing and wind/terrain awareness matter most where field geometry departs from a simple rectangle. For RQ2, MAVLink 2.0 proved reliable under field conditions, sustaining sub-20 ms command latency and >99% packet delivery within the tested 800 m operational range, degrading gracefully rather than failing outright at the 1,500 m maximum range. For RQ3, the NDVI/NDRE pipeline achieved >90% segmentation accuracy across all three crops and a 90.0% weighted F1 for four-class health classification, though the Disease Detected class remains the primary source of error, since early-stage disease and general stress are spectrally similar at this sensor resolution.

Several limitations should be noted. All experiments were conducted in clear weather with wind below 6 m/s; performance in rain, fog, or high wind is untested. The 25-minute flight time caps continuous single-battery coverage at roughly 4.5 hectares, so larger operations require battery-swap protocols that add 7–10 minutes per swap. The health classifier assumes homogeneous canopy structure, and mixed-crop or orchard fields with significant shadowing present additional challenges not evaluated here. Regulatory frameworks for beyond-visual-line-of-sight agricultural UAV operations also remain unsettled in many jurisdictions, and the custom crop-telemetry MAVLink messages used in this system are not yet standardized, limiting interoperability with commercial GCS software.

Future work includes multi-UAV cooperative coverage for large-scale farm monitoring; onboard vegetation-index computation on an NVIDIA Jetson Orin Nano to remove GCS processing latency; thermal imaging for irrigation-stress detection; reinforcement-learning-based adaptive replanning; and standardization of crop-monitoring MAVLink message extensions through the MAVLink working group.

5. Conclusion

This paper presented an integrated system for autonomous quadcopter crop monitoring combining MAVLink-based mission control, a modular ROS2 GCS, and a multispectral crop-health pipeline. The Energy-Optimized coverage path achieved 96.5% coverage efficiency and a 12.4% energy reduction over a standard Boustrophedon baseline, with further gains from wind compensation (1.5–3.1%) and terrain-following (2.1–2.8%). MAVLink 2.0 sustained reliable, low-latency communication under field conditions, and the vegetation-index pipeline achieved over 90% NDVI segmentation accuracy and a 90.0% weighted F1-score for four-class crop-health classification. Together, these results demonstrate practical throughput of 8–12 hectares per flight hour and establish a validated, reproducible architecture for UAV-based precision agriculture monitoring.

Compliance with ethical standards

Acknowledgement.

I am deeply grateful to my co authors, for their dedication and insightful discussions and team work that made this work possible

Disclosure of conflict of interest

There is no conflict of interest.

References

[1] I. A. Hameed, D. Bochtis, and C. A. Sørensen, "An Optimized Field Coverage Planning Approach for Navigation of Agricultural Robots in Fields Involving Obstacle Areas," Int. J. Adv. Robot. Syst., vol. 10, no. 5, art. 231, pp. 1–9, 2013.

[2] T. M. Cabreira, L. B. Brisolara, and P. R. Ferreira Jr., "Survey on Coverage Path Planning with Unmanned Aerial Vehicles," Drones, vol. 3, no. 1, p. 4, Jan. 2019.

[3] A. Koubaa, A. Allouch, M. Alajlan, Y. Javed, A. Belghith, and M. Khalgui, "Micro Air Vehicle Link (MAVLink) in a Nutshell: A Survey," IEEE Access, vol. 7, pp. 87658–87680, 2019.

[4] P. Oettershagen, T. Stastny, T. Mantel, A. Melzer, K. Rudin, P. Gohl, G. Agamennoni, K. Alexis, and R. Siegwart, "Long-Endurance Sensing and Mapping Using a Hand-Launchable Solar-Powered UAV," in Field and Service Robotics, Springer Tracts in Advanced Robotics, vol. 113, Springer, Cham, 2016, pp. 441–454.

[5] E. R. Hunt et al., "A Visible Band Index for Remote Sensing Leaf Chlorophyll Content at the Canopy Scale," Int. J. Appl. Earth Obs. Geoinf., vol. 21, pp. 103–112, Jun. 2013.

[6] A. A. Gitelson, Y. J. Kaufman, and M. N. Merzlyak, "Use of a Green Channel in Remote Sensing of Global Vegetation from EOS-MODIS," Remote Sens. Environ., vol. 58, no. 3, pp. 289–298, Dec. 1996.

[7] W. H. Maes and K. Steppe, "Perspectives for Remote Sensing with Unmanned Aerial Vehicles in Precision Agriculture," Trends Plant Sci., vol. 24, no. 2, pp. 152–164, Feb. 2019.

[8] C. Zhang and J. M. Kovacs, "The Application of Small Unmanned Aerial Systems for Precision Agriculture: A Review," Precis. Agric., vol. 13, no. 6, pp. 693–712, Dec. 2012.

[9] J. Torres-Sanchez et al., "Mapping the 3D Structure of Almond Orchards Using UAV Acquired Photogrammetric Point Clouds and Object-Based Image Analysis," Biosyst. Eng., vol. 176, pp. 172–184, Aug. 2018.

[10] H. Chao, Y. Cao, and Y. Chen, "Autopilots for Small Unmanned Aerial Vehicles: A Survey," Int. J. Control Autom. Syst., vol. 8, no. 1, pp. 36–44, Feb. 2010.

[11] V. Puri, A. Nayyar, and L. Raja, "Agriculture Drones: A Modern Breakthrough in Precision Agriculture," J. Stat. Manag. Syst., vol. 20, no. 4, pp. 507–518, 2017.

[12] A. A. Gitelson, G. P. Keydan, and M. N. Merzlyak, "Three-Band Model for Noninvasive Estimation of Chlorophyll, Carotenoids, and Anthocyanin Contents in Higher Plant Leaves," Geophys. Res. Lett., vol. 33, L11402, Jun. 2006.

[13] I. Sa, Z. Ge, F. Dayoub, B. Upcroft, T. Perez, and C. McCool, "DeepFruits: A Fruit Detection System Using Deep Neural Networks," Sensors, vol. 16, no. 8, p. 1222, Aug. 2016.

[14] P. S. Thenkabail, R. B. Smith, and E. De Pauw, "Hyperspectral Vegetation Indices and Their Relationships with Agricultural Crop Characteristics," Remote Sens. Environ., vol. 71, no. 2, pp. 158–182, Feb. 2000.

[15] A. Matese and S. F. Di Gennaro, "Practical Applications of a Multisensor UAV Platform Based on Multispectral, Thermal and RGB High Resolution Images in Precision Viticulture," Agriculture, vol. 8, no. 7, art. 116, Jul. 2018.